THE JOURNAL OF PHYSICAL CHEMISTRY Letters

pubs.acs.org/JPCL Letter

Two-Dimensional Rare Earth–Gold Intermetallic Compounds on Au(111) by Surface Alloying

Yande Que,* Yuan Zhuang, Ziyuan Liu, Chaoqiang Xu, Bin Liu, Kedong Wang, Shixuan Du, and Xudong Xiao*

Cite This: *J. Phys. Chem. Lett.* 2020, 11, 4107–4112 Read Online

ACCESS | Metrics & More | Article Recommendations | Supporting Information

ABSTRACT: Surface alloying is a straightforward route to control and modify the structure and electronic properties of surfaces. Here, we present a systematic study on the structural and electronic properties of three novel rare earth-based intermetallic compounds, namely, $ReAu_2$ (Re = Tb, Ho, and Er), on Au(111) via directly depositing rare earth metals onto the hot Au(111) surface. Scanning tunneling microscopy/spectroscopy measurements reveal very similar atomic structures and electronic properties, e.g., electronic states and surface work functions, for all these intermetallic compound systems because of the physical and chemical similarities between these rare earth elements. Further, these electronic properties are periodically modulated by the moiré structures caused by the lattice mismatches between $ReAu_2$ and Au(111). These periodically modulated surfaces could serve as templates for the self-assembly of nanostructures. In addition, these two-dimensional rare earth-based intermetallic compounds provide platforms to investigate rare earth-related catalysis, magnetisms, etc. in the lower dimensions.

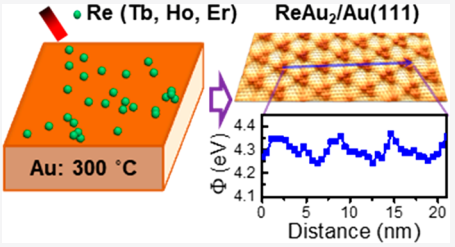

Surface alloying has attracted intense interest among physicists and material scientists because it is a straightforward route to control and modify the structure and electronic properties of surfaces,[1−3] which is fundamentally important for developing technologically relevant materials. First, surface alloying provides an effective way to tune the chemical compositions in the surface layers and thus to tune chemical and physical properties of the relevant materials. For instance, for most catalysts, the active sites are located on or near the surface layers, and thus, the catalytic performance could be tuned by varying the chemical composition in the surface layers.[4−7] Second, the adlayers formed by surface-confined alloying generally have different structures compared with the host materials. Such lattice mismatch results in moiré patterns in these systems, leading to periodically modulated surfaces that could serve as templates for self-assembled growth of nanostructures, *e.g.*, nanocluster or molecules.[8] Further, the periodical modulations in the coupling between the adlayer and the subsequent layer, *e.g.*, substrate, might give rise to new exotic phenomena.

Lanthanide rare earth-based intermetallic compounds on noble metal surfaces are good examples of periodically modulated surfaces by surface alloying. Deposition of gadolinium (Gd) on hot Au(111) or Ag(111) gives rise to the formation of long-range ordered $GdAu_2$ and $GdAg_2$.[9,10] The lattice mismatches in these systems results in periodically modulated moiré structures, leading to electronic modulations in these systems.[11,12] The structurally robust moiré lattices in $GdAu_2$ have been reported as templates for well-aligned organic nanowires[6] and dense arrays of Co nanodots.[13−15] In addition, two-dimensional ferromagnetic orders have been reported in these systems mainly originating from the 4*f* electrons in the rare earth atoms.[10,16] The Curie temperatures are ∼10 K and ∼80 K for $GdAu_2$ and $GdAg_2$, respectively. Further, the reduced dimensionality gives rise to new exotic states in these systems. For instance, Weyl nodal lines were observed in $GdAg_2$/Ag(111) by angle-resolved photoemission spectroscopy (ARPES) combined with first-principles calculations.[17]

Besides Gd, other lanthanide element-based intermetallic compounds by the same or similar approaches have also been reported, like $LaAu_2$,[18] $CeAu_2$,[18] and $ErCu_2$.[19] In this work, we apply the high-temperature growth procedure to another three lanthanide elements [terbium (Tb), holmium (Ho), and erbium (Er)] on Au(111). These systems are particularly attractive because these rare earth elements have similar chemical bonds but have different 4*f* electrons compared with La, Ce, and Gd, thus leading to different magnetisms. Further, these elements have different nuclear spins and nuclear magnetic moments, which might give rise to new magnetic phenomena due to the coupling between the nuclear and electron spins. Thus, these two-dimensional systems provide platforms to investigate rare earth related magnetisms. Via scanning tunneling microscopy (STM), we unveil that all these

Received: March 29, 2020
Accepted: May 5, 2020
Published: May 5, 2020

rare earth elements form very similar structures in the forms of $TbAu_2$, $HoAu_2$, and $ErAu_2$, similar to the reported rare earth-based intermetallic compound on Au(111). In addition, scanning tunneling spectroscopy (STS) measurement reveals very similar electronic properties in these intermetallic compounds, including local density of states and the surface work function. Further, the electronic states as well as the surface work function are periodically modulated by the moiré structures originating from the lattice mismatch.

Deposition of rare earth metals onto clear Au(111) surfaces at 300 °C leads to the formation of well-ordered rare earth−gold surface alloys. Figure 1a presents a large-scale topographic image of $TbAu_2$ formed on Au(111) (for details on the determination of the stoichiometry, see section 1 in the Supporting Information), showing a highly ordered hexagonal superstructure, namely moiré structure, with lattice constants of 3.68 ± 0.10 nm. The inset in Figure 1a clearly shows three different regions within each unit cell of the moiré structure: dark spot, brightest spot, and the second brightest spot (termed valley, hill, and bridge regions, respectively, in the following). The apparent height differences are revealed by the height profile across the unit cells, as shown in Figure 1b. The peaks and valleys in the height profile correspond to the hill and valley regions, whereas the shoulders adjacent to the peaks correspond to the bridge region. The overall height differences vary with the sample bias (see Figure S2 in the Supporting Information) from ∼60 to ∼40 pm, revealing these height differences are contributed from the geometric corrugation as well as electronic modulation, where the former is dominant.

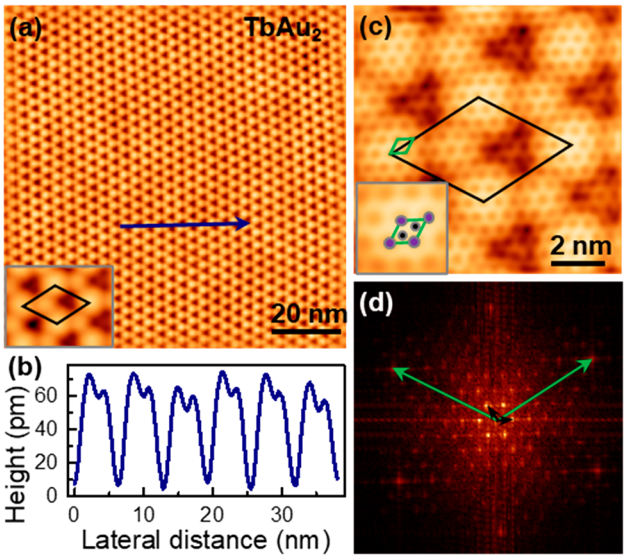

Figure 1. STM topographic images of $TbAu_2$. (a) Large-scale and (c) atomically resolved STM images of $TbAu_2$ on Au(111), respectively. (b) Height profile along the blue arrow in panel a. (d) FFT of atomically resolved STM image of $TbAu_2$, the same area as in panel c but with dimensions of 30 × 30 nm^2. Inset in panel a shows its zoomed-in image, and the black diamond in the inset denotes the unit cell. Green and black diamonds in panel d denote the unit cell of the $TbAu_2$ and the moiré lattices. The inset in panel c shows its zoomed-in image, where the purple and black solid circles represent Tb and Au atoms, respectively. Green and black arrowed lines in panel d denote the reciprocal lattice vectors of the $TbAu_2$ and the moiré structures, respectively. Tunneling conditions for panel a are U = 2.0 V and I = 200 pA; for panel c, U = 0.5 V and I = 2.0 nA.

Besides the moiré structure, the atomically resolved STM image (Figure 1c) shows a honeycomb structure with a lattice constant of 5.4 ± 0.2 Å, a factor of $4\sqrt{3}$ smaller than that of moiré structure within the error limit. The unit cell is sketched out in the zoomed-in image (inset in Figure 1c), showing that only Au atoms were resolved in the atomic-resolution image. It should be noted that only Tb atoms could be resolved under some tunneling conditions. The corresponding fast Fourier transform (FFT) image present in Figure 1d shows the patterns for these two hexagonal structures, where the green and black vectors indicate the reciprocal lattices for the atomic lattice and moiré lattice. The angle between these two vectors was measured to be 30.0 ± 0.2°. Thus, the moiré structure is $4\sqrt{3} \times 4\sqrt{3}$-R30° respective to the $TbAu_2$ lattice.

To identify the relation between the $TbAu_2$ and the Au substrate, we carried out low-energy electron diffraction (LEED) measurements. For the clean Au(111), the pattern shows only six spots, as shown in Figure 2a, indicating the 3-fold symmetry as well as the cleanness of the Au substrate. In contrary, Figure 2b shows a set of moiré pattern for $TbAu_2$/Au(111). Compared with the pattern for clean Au(111), it reveals the angle of 30° between lattices of $TbAu_2$ and the moiré structure, in consistence with the atomic resolution STM results. Besides, the lattice vectors of the moiré structure are parallel to those of Au(111), and hence, the angle between the lattices of $TbAu_2$ and Au(111) is 30°. Therefore, combined with the STM results, the moiré structure could be modeled as $4\sqrt{3} \times 4\sqrt{3}$-R30° $TbAu_2$ on 13 × 13 Au(111).

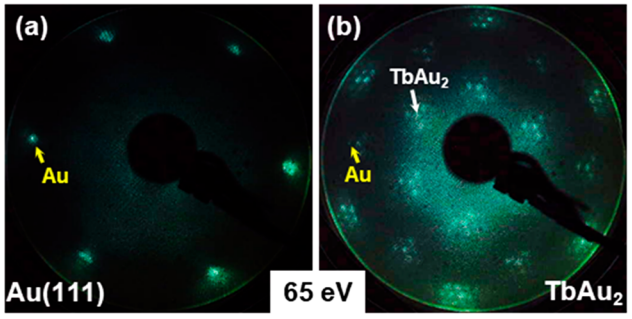

Figure 2. LEED patterns of (a) clean Au(111) and (b) $TbAu_2$/Au(111).

Similar structures have been reported in other rare earth metal surface alloys, like $GdAu_2$/Au(111),[20] $GdAg_2$/Ag-(111),[10] $LaAu_2$/Au(111),[18] $CeAu_2$/Au(111),[18] $ErCu_2$/Cu-(111),[19] and so on. Naturally, the question becomes whether other lanthanide metals have similar surface alloys on noble metal surfaces. Therefore, we employed the same approach for another two lanthanide elements, Ho and Er. Figure 3 presents the STM results for the as-grown $HoAu_2$ formed on Au(111) by deposition of Ho onto the Au(111) at 300 °C. It shows a highly ordered hexagonal moiré structure (Figure 3a) with a periodicity of 3.66 ± 0.05 nm. The atomic-resolution STM image in Figure 3b reveals the atomic lattice superimposed with the moiré structure. The unit cell is sketched out in the zoomed-in image (inset in Figure 3b), showing only Ho atoms are resolved. The lattice constant for $HoAu_2$ was measured to be 5.4 ± 0.1 Å, a factor of $4\sqrt{3}$ smaller than that of the moiré structure within the error limit. The corresponding FFT image present in Figure 3c shows the patterns for these two hexagonal structures. The unit cells in Figure 3b and the

https://dx.doi.org/10.1021/acs.jpclett.0c00981
J. Phys. Chem. Lett. 2020, 11, 4107−4112

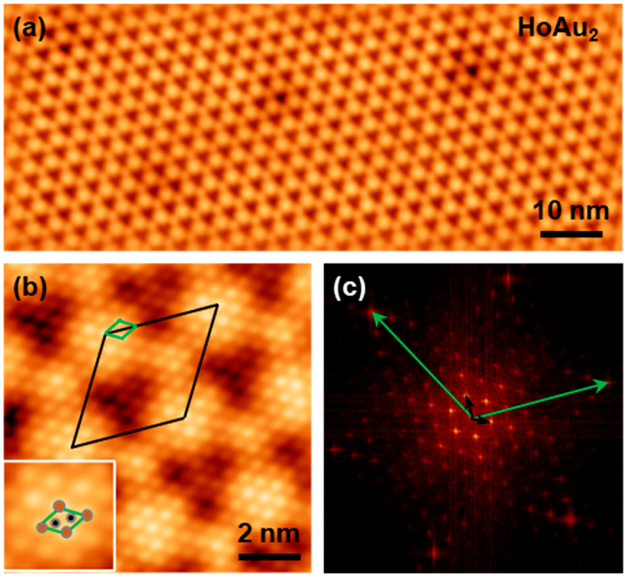

Figure 3. STM topographic images of $HoAu_2$. (a) Large-scale and (b) atomically resolved STM images of $HoAu_2$ on Au(111), respectively. The inset in panel b shows its zoomed-in image, where the orange and black solid circles represent Ho and Au atoms, respectively. Green and black diamonds in panel b represent the unit cells of $HoAu_2$ and the moiré structures, respectively. (c) FFT image of atomically resolved STM image of $HoAu_2$, the same area as in panel c but with dimensions of 40 × 40 nm^2. Green and black arrowed lines in panel c denote the reciprocal lattice vectors of the $HoAu_2$ and the moiré structures, respectively. Tunneling conditions for panel a U = 2.0 V, I = 500 pA; for panel b, U = 0.1 V, I = 500 pA.

reciprocal lattice vectors in Figure 3c imply that the moiré lattice is $4\sqrt{3} \times 4\sqrt{3}$-R30° with respect to the atomic lattice of $HoAu_2$.

Similar results were observed for $ErAu_2$ on Au(111) formed by deposition of Er atoms onto a hot (300 °C) Au(111) substrate, as shown in Figure 4. The large-scale STM image (Figure 4a) reveals the long-range ordered moiré structures of $ErAu_2$/Au(111) with periodicity of 3.76 ± 0.04 nm. The atomic-resolution STM image in Figure 4b reveals the atomic lattice superimposed with the moiré structure. The unit cell is sketched out in the zoomed-in image (inset in Figure 4b), showing only the Au atoms are resolved. The lattice constant for $ErAu_2$ was measured to be 5.4 ± 0.1 Å, a factor of $4\sqrt{3}$ smaller than that of moiré structure within the error limit. The corresponding FFT image present in Figure 4c shows the patterns for these two hexagonal structures. The unit cells in Figure 4b and the reciprocal lattice vectors in Figure 4c imply that the moiré lattice is $4\sqrt{3} \times 4\sqrt{3}$-R30° with respect to the atomic lattice of $ErAu_2$. Therefore, $TbAu_2$, $HoAu_2$, and $ErAu_2$ on Au(111) have almost the same structures including the atomic lattices and moiré lattices, which is consistent with the physical and chemical similarities between Tb, Ho, and Er elements.

For better comparison, we listed the structures for all the reported rare earth-based intermetallic compounds on Au(111) formed by surface alloying in Table 1. A hexagonal surface alloy could be formed for all the listed lanthanum elements, which is consistent with the similarities of the lanthanum elements. The lattice constant for these hexagonal surface alloys slightly varies from 5.3 to 5.5 Å because of the slight differences in the atom size for the lanthanide elements.

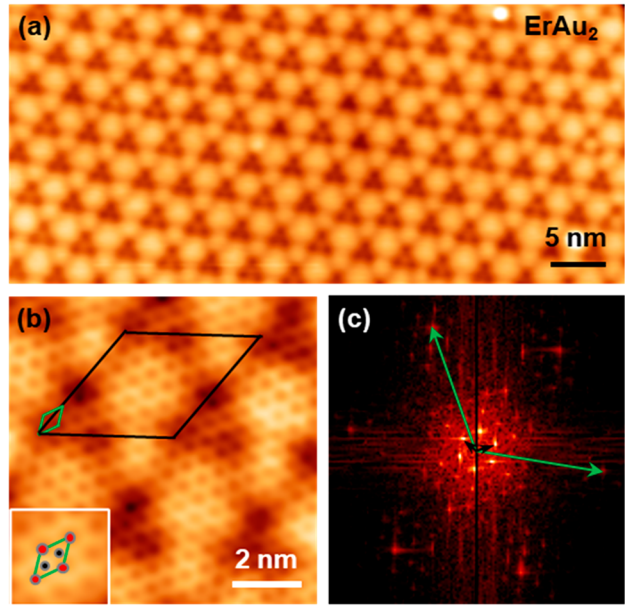

Figure 4. STM topographic images of $ErAu_2$. (a) Large-scale and (b) atomically resolved STM images of $ErAu_2$ on Au(111), respectively. Inset in b shows its zoomed-in image, where the red and black solid circles represent Er and Au atoms, respectively. Green and black diamonds in panel b represent the unit cells of $ErAu_2$ and the moiré structures, respectively. (c) FFT image of atomically resolved STM image of $ErAu_2$, the same area as panel b but with dimensions of 25 × 25 nm^2. Green and black arrowed lines in panel c denote the reciprocal lattice vectors of the $ErAu_2$ and the moiré structures, respectively. Tunneling conditions for panel a $U = -2.0$ V and $I = 200$ pA; for panel b, $U = 5$ mV and $I = 2.5$ nA.

Table 1. Structures for Rare-Earth-Based Intermetallic Compounds on Au(111)

$REAu_2$	structure	atomic lattice (Å)	moiré lattice (nm)	references
$LaAu_2$	hexagonal	5.3	3.2	18
$CeAu_2$	hexagonal	5.4	3.3	18
$GdAu_2$	hexagonal	5.4−5.5	3.6−3.8	12, 16, 20
$TbAu_2$	hexagonal	5.4	3.68	this work
$HoAu_2$	hexagonal	5.4	3.66	this work
$ErAu_2$	hexagonal	5.4	3.76	this work

Accordingly, the lattice constant for the moiré structure varies from 3.2 to 3.8 nm because of the difference in the lattice mismatch between the surface alloy and Au(111) substrate. The moiré structure with different periodicities might be used to tune the growth of nanoclusters or self-assemblies of molecules.

So far, we have investigated the structures of the rare earth gold surface alloys formed on Au(111) including $TbAu_2$, $HoAu_2$, and $ErAu_2$. They have almost the same hexagonal structures with the same lattice constant, thus giving rise to the moiré structures with the same periodicity within the error limit. In the following, we will employ STS measurement to unravel the electronic properties of the rare earth gold surface alloys, mainly the $TbAu_2$ on Au(111), modulated by the moiré structures.

Figure 5a presents the differential conductance spectra of $TbAu_2$ taken at three different regions within the unit cell of the moiré structure. All the spectra show similar features with a pronounced peak around 0.6 eV above the Fermi level. Similar

https://dx.doi.org/10.1021/acs.jpclett.0c00981
J. Phys. Chem. Lett. 2020, 11, 4107−4112

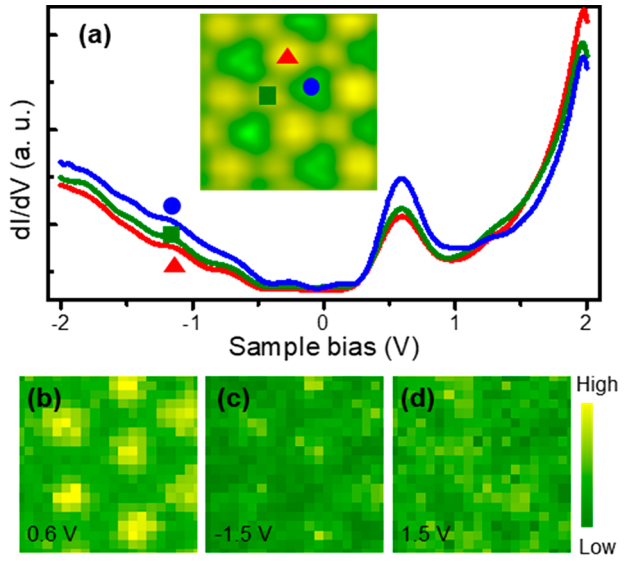

Figure 5. STS differential conductance spectra and mappings of $TbAu_2$/Au(111). (a) dI/dV spectra of $TbAu_2$ taken at three different regions (indicated in the inset STM image with area of 9 × 9 nm^2) within the unit cell of the moiré structure of $TbAu_2$. (b−d) Differential conductance mappings of $TbAu_2$ at sample bias at 0.6, −1.5, and 1.5 V, respectively. The corresponding topographic image is present as the inset in panel a. The tunneling conditions for the spectra and mappings are U = 2.0 V and I = 1.0 nA.

features are observed in the other rare earth metal surface alloys including $HoAu_2$/Au(111) and $ErAu_2$/Au(111) (see Figures S3 and S4 in the Supporting Information) and $ErCu_2$/Cu(111). The STS spectra for these systems show a pronounced peak around 0.6 eV, implying that this peak is mainly contributed from the rare earth atoms in the alloys, slightly depending on the type of lanthanide atoms. Our theoretical calculations reveal that such a state is mainly contributed from the d states of Tb atoms for the $TbAu_2$/Au(111) (see Figure S5 in the Supporting Information). In the $ErCu_2$,[19] the peak around 0.6 eV is contributed from the Er d state mixed with Cu p state and d state confirmed by first-principles calculations. In addition, the energy for this peak is position-dependent because of the moiré modulations. In contrast, for $TbAu_2$ in this work, no energy shift was observed for the pronounced peak at ∼0.6 eV at different regions, which might be due to the different coupling strength with the substrate. Instead, the intensity of this peak varies within the unit cell of the moiré structures. It shows higher intensity of this peak for the spectrum taken at the dark regions or the valley sites than the other two regions, indicating the higher local density of states (LDOS) at the valley regions within the unit cell of the moiré structures. To further confirm such position dependence of the LDOS, we mapped the STS differential conductance over the unit cells of the moiré structures. As shown in Figure 5b, the dI/dV mapping at the energy of 0.6 eV clearly reveals the higher LDOS at the valley regions within the unit cell of the moiré structures, indicating the electronic state at 0.6 eV is modulated by the moiré structures. In addition, the spectra show overall slightly higher intensity at the valley regions below the energy level of ∼1.2 eV than that in the hill and bridge regions, whereas a slightly lower intensity is shown above ∼1.2 eV. The dI/dV mappings at −1.5 eV (Figure 5c) and 1.5 eV (Figure 5d) reveal the reversed contrast for the valley regions, illustrating the relative change in the LDOS due to the moiré modulations.

Further, we employed the STS in the distance−voltage $z(V)$ mode to investigate the electronic structures of the $TbAu_2$/Au(111), which has been employed to study the field-emission resonance (FER) phenomenon.[21,22] FER provides an ideal playground for the study of fundamental physical properties like surface work function.[23] Figure 6a presents the dz/dV spectra of $TbAu_2$/Au(111) and clean Au(111) for comparison. On clean Au(111), it shows a pronounced step around 3.5 eV, corresponding the upper edge of the Au L-gap.[24,25] Besides, it reveals 7 FER states within the energy range to 10 eV. The first FER state locates at ∼5.2 eV, which could be used as the reference for the surface work function. The more accurate surface work function can be calculated by the following equation based on a 1D tunneling junction model:[26]

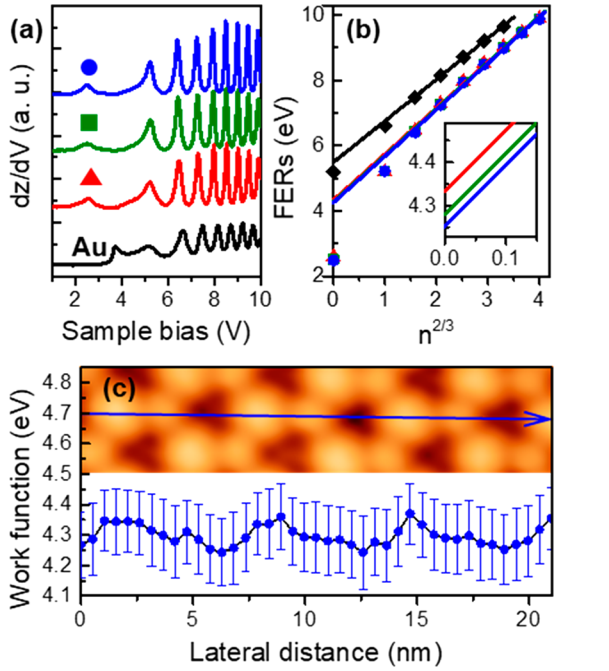

Figure 6. Surface work function of $TbAu_2$/Au(111). (a) dz/dV spectra of Au(111) and $TbAu_2$ taken at the featured regions within the unit cell of the moiré structures. The solid triangle, square, and circle indicate the positions where the spectra were taken, which are the same as those in Figure 3a. (b) Relations between the energy and index of the FER states. The energies of the FER states were extracted from the spectra in panel a. The solid lines are the linearly fitted curves for $n \geq 2$. The intersects at n = 0 are magnified and shown in the inset. (c) Surface work function profile of $TbAu_2$ along the blue arrow in the top panel. All the spectra were taken at the tunneling current of 20 pA to reduce the Stark shift in the spectra.

$$E_n = \Phi + \left(\frac{3\pi\hbar}{2\sqrt{2m}}F\right)^{2/3} n^{2/3} \quad (1)$$

where E_n is the energy of the n^{th} FER state, Φ is the local surface work function, $\hbar$ is the reduced Planck's constant, m is the effective mass of surface charge, and F is the electric field. The surface work function of Au(111) was calculated to be 5.49 ± 0.09 eV by fitting the FER states according to eq 1 (Figure 6b), which agrees well with the reported value (5.35 eV).[27]

https://dx.doi.org/10.1021/acs.jpclett.0c00981
J. Phys. Chem. Lett. 2020, 11, 4107−4112

On $TbAu_2$/Au(111), all the spectra show 9 FER states within the scanning range of 10 eV with a weak dependence with position within the unit cell of the moiré structures. The first FER state locates around 2.6 eV (vs 5.2 eV for Au), indicating a reduction in the surface work function compared with clean Au(111). By fitting the FER states according the eq 1, as shown in Figure 6b, the surface work functions on $TbAu_2$/Au(111) were extracted to be 4.33 ± 0.11, 4.28 ± 0.11, and 4.25 ± 0.12 eV for the hill, bridge, and valley regions, respectively. These values are between the work functions of pure Tb (~3.1 eV) and gold (~5.4 eV), which is rational according to the composition dependence of work function in binary metal alloys.[28] Moreover, similar reduction in work function has been observed in the $GdAu_2$/Au(111) system by photoemission spectroscopy measurement.[6]

To confirm that the slight differences in the surface work functions of $TbAu_2$/Au(111) on different regions are caused by the modulation of the moiré structures rather than measurement uncertainty, we carried out the dz/dV line-mapping crossing several unit cells of the moiré structures. Figure 6c presents the surface work function profile along the blue arrow crossing three unit cells of the moiré structures of $TbAu_2$/Au(111). The surface work function of $TbAu_2$/Au(111) periodically varies with the same period of the moiré structures, revealing that the surface work function of $TbAu_2$/Au(111) is modulated by the moiré structures consistent with the previous dI/dV results. It is worth noting that the surface work function of $HoAu_2$/Au(111) and $ErAu_2$/Au(111) was measured to be around 4.3 eV and modulated by the moiré structures too (see Figures S7 and S8 in the Supporting Information).

In summary, we have investigated the structural and electronic properties of three novel rare earth-based intermetallic compounds, namely $TbAu_2$, $HoAu_2$, $ErAu_2$, on Au(111) via STM/STS. The deposition of rare earth metals onto the hot Au(111) surface gives rise to the formation of long-range ordered monolayers of intermetallic compounds. Atomically resolved STM images reveal hexagonal lattices with lattice constant of ~5.4 Å for all these monolayers on Au(111), superimposed with moiré structures. The lattice constant for the moiré structures slightly depends on the type of lanthanide atoms, in the range of 3.66−3.76 nm. The moiré structures could be modeled as $4\sqrt{3} \times 4\sqrt{3}$-R30° $ReAu_2$ (Re = Tb, Ho, and Er) on 13 × 13 Au(111). STS measurement illustrated the very similar electronic structures for all these intermetallic compound systems with a pronounced state at ~0.6 eV above the Fermi level. Besides, the FER spectra reveal a significant reduction in the surface work function after the formation of intermetallic compounds. Further, the electronic states and surface work function are periodically modulated by the moiré structures. These periodically modulated surfaces could serve as templates for the self-assembly of organic molecules or nanoclusters. In addition, these two-dimensional rare earth-based intermetallic compounds provide platforms to investigate the rare earth related catalysis, magnetisms, etc., in the lower dimensions.

MATERIALS AND METHODS

Sample Preparation. Clean Au(111) surfaces were prepared by repeated cycles of Ar^+ sputtering (600 eV) and annealing at 450 °C. The cleanness of the Au(111) surface was verified by STM topographic images. Rare earth metals (Tb, Ho, and Er) were deposited onto clean Au(111) via a commercial e-beam evaporator (EFM-3T, omicron). During the deposition, the Au(111) substrate was kept at 300 °C to stimulate the formation of well-ordered rare earth−gold surface alloys.

All the experiments were carried out in an UHV LT-STM system with a base pressure better than 2×10^{-10} mbar. The sample was directly transferred to the STM without breaking the UHV environment after the growth of the surface alloys. For the LEED measurement, samples were transferred to a separate UHV VT-STM system equipped with a LEED setup using a homemade UHV suitcase. The cleanness of the sample after the transfer was verified by STM imaging.

LEED and STM/STS Measurement. LEED measurements were conducted at room temperature with an incident electron energy of 65 eV. The STM images were acquired in a constant-current mode at the temperature of liquid nitrogen (~78 K) using an electrochemically etched tungsten tip and all the labeled bias voltages referred to the sample against tip. All the STM images were postprocessed by the WSxM software.[29] The dI/dV (dz/dV) spectra and mapping were obtained by numerical derivation of $I(V)$ [$z(V)$] spectra. Prior to the spectroscopic measurement, the STM tip was calibrated against the surface states of the Au(111) or Cu(111) surfaces.

ASSOCIATED CONTENT

Supporting Information

The Supporting Information is available free of charge at https://pubs.acs.org/doi/10.1021/acs.jpclett.0c00981.

Details of determination of stoichiometry of the rare earth−gold intermetallic compounds, bias-dependent height corrugations in $TbAu_2$/Au(111), electronic properties of $HoAu_2$/Au(111) and $ErAu_2$/Au(111), band structures of $TbAu_2$, Stark shift in the FERs of $TbAu_2$/Au(111), surface work function of $HoAu_2$/Au(111) and $ErAu_2$/Au(111) (PDF)

AUTHOR INFORMATION

Corresponding Authors

Yande Que − *Department of Physics, the Chinese University of Hong Kong, Hong Kong, China*; orcid.org/0000-0002-5267-4985; Email: ydque@phy.cuhk.edu.hk

Xudong Xiao − *Department of Physics, the Chinese University of Hong Kong, Hong Kong, China*; orcid.org/0000-0003-0551-1144; Email: xdxiao@phy.cuhk.edu.hk

Authors

Yuan Zhuang − *Department of Physics, the Chinese University of Hong Kong, Hong Kong, China*

Ziyuan Liu − *Institute of Physics and University of Chinese Academy of Sciences, Chinese Academy of Sciences, Beijing 100190, China*

Chaoqiang Xu − *Department of Physics, the Chinese University of Hong Kong, Hong Kong, China*; orcid.org/0000-0001-8561-8974

Bin Liu − *Department of Physics, the Chinese University of Hong Kong, Hong Kong, China*

Kedong Wang − *Department of Physics, Southern University of Science and Technology, Shenzhen, Guangdong 518055, China*

Shixuan Du − *Institute of Physics and University of Chinese Academy of Sciences, Chinese Academy of Sciences, Beijing 100190, China*; orcid.org/0000-0001-9323-1307

Complete contact information is available at: https://pubs.acs.org/10.1021/acs.jpclett.0c00981

https://dx.doi.org/10.1021/acs.jpclett.0c00981
J. Phys. Chem. Lett. 2020, 11, 4107−4112

Notes

The authors declare no competing financial interest.

■ ACKNOWLEDGMENTS

This work was supported by the Research Grant Council of Hong Kong (No. 404613), the Direct Grant for Research of CUHK (No. 4053306 and No. 4053348), the National Natural Science Foundation of China (No. 11574128), and the MOST 973 Program (No. 2014CB921402).

■ REFERENCES

(1) Ast, C. R.; Henk, J.; Ernst, A.; Moreschini, L.; Falub, M. C.; Pacilé, D.; Bruno, P.; Kern, K.; Grioni, M. Giant Spin Splitting through Surface Alloying. *Phys. Rev. Lett.* **2007**, *98*, 186807.

(2) Chen, H.; Wang, R.; Huang, R.; Zhao, C.; Li, Y.; Gong, Z.; Yao, Y.; Cui, Y.; Yang, F.; Bao, X. Surface and Subsurface Structures of the Pt-Fe Surface Alloy on Pt(111). *J. Phys. Chem. C* **2019**, *123*, 17225−17231.

(3) Sadhukhan, P.; Barman, S.; Roy, T.; Singh, V. K.; Sarkar, S.; Chakrabarti, A.; Barman, S. R. Electronic Structure of Au-Sn Compounds Grown on Au(111). *Phys. Rev. B: Condens. Matter Mater. Phys.* **2019**, *100*, 235404.

(4) Nikolla, E.; Schwank, J.; Linic, S. Promotion of the Long-Term Stability of Reforming Ni Catalysts by Surface Alloying. *J. Catal.* **2007**, *250*, 85−93.

(5) Stamenkovic, V. R.; Mun, B. S.; Arenz, M.; Mayrhofer, K. J. J.; Lucas, C. A.; Wang, G.; Ross, P. N.; Markovic, N. M. Trends in Electrocatalysis on Extended and Nanoscale Pt-Bimetallic Alloy Surfaces. *Nat. Mater.* **2007**, *6*, 241−247.

(6) Abadía, M.; Ilyn, M.; Piquero-Zulaica, I.; Gargiani, P.; Rogero, C.; Ortega, J. E.; Brede, J. Polymerization of Well-Aligned Organic Nanowires on a Ferromagnetic Rare-Earth Surface Alloy. *ACS Nano* **2017**, *11*, 12392−12401.

(7) Zhang, Q.; Kusada, K.; Wu, D.; Yamamoto, T.; Toriyama, T.; Matsumura, S.; Kawaguchi, S.; Kubota, Y.; Kitagawa, H. Selective Control of Fcc and Hcp Crystal Structures in Au-Ru Solid-Solution Alloy Nanoparticles. *Nat. Commun.* **2018**, *9*, 510.

(8) Fuhr, J. D.; Robino, L. I.; Rodríguez, L. M.; Verdini, A.; Floreano, L.; Ascolani, H.; Gayone, J. E. 2D Cu-TCNQ Metal-Organic Networks Induced by Surface Alloying. *J. Phys. Chem. C* **2020**, *124*, 416−424.

(9) Corso, M.; Verstraete, M. J.; Schiller, F.; Ormaza, M.; Fernández, L.; Greber, T.; Torrent, M.; Rubio, A.; Ortega, J. E. Rare-Earth Surface Alloying: A New Phase for $GdAu_2$. *Phys. Rev. Lett.* **2010**, *105*, 016101.

(10) Ormaza, M.; Fernández, L.; Ilyn, M.; Magana, A.; Xu, B.; Verstraete, M. J.; Gastaldo, M.; Valbuena, M. A.; Gargiani, P.; Mugarza, A.; et al. High Temperature Ferromagnetism in a $GdAg_2$ Monolayer. *Nano Lett.* **2016**, *16*, 4230−4235.

(11) Correa, A.; Xu, B.; Verstraete, M. J.; Vitali, L. Strain-Induced Effects in the Electronic and Spin Properties of a Monolayer of Ferromagnetic $GdAg_2$. *Nanoscale* **2016**, *8*, 19148−19153.

(12) Correa, A.; Camellone, M. F.; Barragan, A.; Kumar, A.; Cepek, C.; Pedio, M.; Fabris, S.; Vitali, L. Self-Texturizing Electronic Properties of a 2-Dimensional $GdAu_2$ Layer on Au(111): The Role of out-of-Plane Atomic Displacement. *Nanoscale* **2017**, *9*, 17342−17348.

(13) Fernández, L.; Blanco-rey, M.; Ilyn, M.; Vitali, L.; Magana, A.; Correa, A.; Ohresser, P.; Ortega, J. E.; Ayuela, A.; Schiller, F. Co Nanodot Arrays Grown on a $GdAu_2$ Template: Substrate/Nanodot Antiferromagnetic Coupling. *Nano Lett.* **2014**, *14*, 2977−2981.

(14) Cavallin, A.; Fernández, L.; Ilyn, M.; Magaña, A.; Ormaza, M.; Matena, M.; Vitali, L.; Ortega, J. E.; Grazioli, C.; Ohresser, P.; et al. Magnetism and Morphology of Co Nanocluster Superlattices on $GdAu_2$/Au(111)− (13 × 13). *Phys. Rev. B: Condens. Matter Mater. Phys.* **2014**, *90*, 235419.

(15) Fernández, L.; Ilyn, M.; Magaña, A.; Vitali, L.; Ortega, J. E.; Schiller, F. Growth of Co Nanomagnet Arrays with Enhanced Magnetic Anisotropy. *Adv. Sci.* **2016**, *3*, 1600187.

(16) Bazarnik, M.; Abadia, M.; Brede, J.; Hermanowicz, M.; Sierda, E.; Elsebach, M.; Hänke, T.; Wiesendanger, R. Atomically Resolved Magnetic Structure of a Gd-Au Surface Alloy. *Phys. Rev. B: Condens. Matter Mater. Phys.* **2019**, *99*, 174419.

(17) Feng, B.; Zhang, R. W.; Feng, Y.; Fu, B.; Wu, S.; Miyamoto, K.; He, S.; Chen, L.; Wu, K.; Shimada, K.; et al. Discovery of Weyl Nodal Lines in a Single-Layer Ferromagnet. *Phys. Rev. Lett.* **2019**, *123*, 116401.

(18) Ormaza, M.; Fernández, L.; Lafuente, S.; Corso, M.; Schiller, F.; Xu, B.; Diakhate, M.; Verstraete, M. J.; Ortega, J. E. $LaAu_2$ and $CeAu_2$ Surface Intermetallic Compounds Grown by High-Temperature Deposition on Au(111). *Phys. Rev. B: Condens. Matter Mater. Phys.* **2013**, *88*, 125405.

(19) Xu, C.; Bao, K.; Que, Y.; Zhuang, Y.; Shao, X.; Wang, K.; Zhu, J.; Xiao, X. A Two-Dimensional $ErCu_2$ Intermetallic Compound on Cu(111) with Moiré-Pattern-Modulated Electronic Structures. *Phys. Chem. Chem. Phys.* **2020**, *22*, 1693−1700.

(20) Corso, M.; Fernández, L.; Schiller, F.; Ortega, J. E. Au(111)-Based Nanotemplates by Gd Alloying. *ACS Nano* **2010**, *4*, 1603−1611.

(21) Becker, R. S.; Golovchenko, J. A.; Swartzentruber, B. S. Electron Interferometry at Crystal Surfaces. *Phys. Rev. Lett.* **1985**, *55*, 987−990.

(22) Binnig, G.; Frank, K. H.; Fuchs, H.; Garcia, N.; Reihl, B.; Rohrer, H.; Salvan, F.; Williams, A. R. Tunneling Spectroscopy and Inverse Photoemission: Image and Field States. *Phys. Rev. Lett.* **1985**, *55*, 991−994.

(23) Xu, C.; Que, Y.; Zhuang, Y.; Liu, B.; Ma, Y.; Wang, K.; Xiao, X. Manipulating the Edge of a Two-Dimensional MgO Nanoisland. *J. Phys. Chem. C* **2019**, *123*, 19619−19624.

(24) LaShell, S.; McDougall, B. A.; Jensen, E. Spin Splitting of an Au(111) Surface State Band Observed with Angle Resolved Photoelectron Spectroscopy. *Phys. Rev. Lett.* **1996**, *77*, 3419−3422.

(25) Pan, Y.; Benedetti, S.; Nilius, N.; Freund, H.-J. Change of the Surface Electronic Structure of Au(111) by a Monolayer MgO(001) Film. *Phys. Rev. B: Condens. Matter Mater. Phys.* **2011**, *84*, 075456.

(26) König, T.; Simon, G. H.; Rust, H.-P.; Heyde, M. Work Function Measurements of Thin Oxide Films on Metals—MgO on Ag(001). *J. Phys. Chem. C* **2009**, *113*, 11301−11305.

(27) De Renzi, V.; Rousseau, R.; Marchetto, D.; Biagi, R.; Scandolo, S.; del Pennino, U. Metal Work-Function Changes Induced by Organic Adsorbates: A Combined Experimental and Theoretical Study. *Phys. Rev. Lett.* **2005**, *95*, 046804.

(28) Ishii, R.; Matsumura, K.; Sakai, A.; Sakata, T. Work Function of Binary Alloys. *Appl. Surf. Sci.* **2001**, *169*−*170*, 658−661.

(29) Horcas, I.; Fernández, R.; Gómez-Rodríguez, J. M.; Colchero, J.; Gómez-Herrero, J.; Baro, A. M. WSXM: A Software for Scanning Probe Microscopy and a Tool for Nanotechnology. *Rev. Sci. Instrum.* **2007**, *78*, 013705.

https://dx.doi.org/10.1021/acs.jpclett.0c00981
J. Phys. Chem. Lett. 2020, 11, 4107−4112